Performance Metrics for Oceanographic Surveys With Autonomous Underwater Vehicles

J. Scott Willcox, *Member, IEEE*, James G. Bellingham, Yanwu Zhang, *Member, IEEE*, and
Arthur B. Baggeroer, *Fellow, IEEE*

Abstract—The focus of this paper is the development of tools to facilitate the effective use of AUVs to survey small-scale oceanographic processes. A fundamental difficulty in making oceanographic surveys with autonomous underwater vehicles (AUVs) is the coupling of space and time through the AUV survey trajectory. Combined with the finite velocity and battery life of an AUV, this imposes serious constraints on the extent of the survey domain and on the spatial and temporal survey resolutions. In this paper, we develop a quantitative survey error metric which accounts for errors due to both spatial undersampling and temporal evolution of the sample field. The accuracy of the survey error metric is established through surveys of a simulated oceanographic process. Using the physical constraints of the platform, we also develop the "survey envelope" which delineates a region of survey parameter space within which an AUV can sucessfully complete a mission. By combining the survey error metric with the survey envelope, we create a graphical survey analysis tool which can be used to gain insight into the AUV survey design problem. We demonstrate the application of the survey analysis tool with an examination of the impact of certain survey design and parameters on surveys of a simple oceanographic process.

Index Terms—Autonomous underwater vehicle, AUV, survey design, survey error.

I. INTRODUCTION

CAPABILITIES for synoptic observation of dynamic processes in the ocean are needed. To obtain synoptic data from *in situ* observations, a survey system must be capable of mapping an ocean structure faster than significant changes in this structure occur. Unfortunately, the wide range of scales of both temporal and spatial variability found in these processes makes surveying dynamic phenomena in the world's oceans problematic [1]. For many traditional methods of oceanographic sampling, the requirement of synopticity must be relaxed due to physical, economic, and/or operational limitations of the sampling platforms [2].

The present generation of oceanographic field programs are fundamentally limited by too few measurements, taken too slowly, at too great a cost. One approach to provide more economical access to the ocean is to use many small, low-cost autonomous underwater vehicles (AUVs) [3]–[5], Fig. 1, to accomplish surveys of dynamic oceanographic phenomena [6]. With such devices, near-synoptic surveys become economically feasible and are well suited to the study of some oceanographic phenomena. However, the advent of such capabilities creates a demand for quantitative tools for optimizing their use.

The current state of practice in AUV-based surveying is primarily oriented toward track-line surveys of static phenomena such as sea floor bathymetry [7], magnetism [8], and sonar [9] or video imagery. Several authors have contributed to a small but growing literature in AUV-based adaptive surveying [10]–[12]. However, these authors have ignored the intramission temporal evolution of the processes of interest to make their problems tractable. Environment-dependent [13] and data-adaptive [14] navigation algorithms to insure complete sonar swath coverage of predefined survey areas have also been developed for potential use on AUVs. While the later of these two algorithms can react to time-varying changes in the environment, both algorithms assume that the underlying process of interest (i.e., sea floor topography or imagery) does not change over the duration of the survey.

To adequately sample dynamic ocean phenomena, we need to find ways of allocating our scarce observational resources so as to maximize the information content of the collected data. Because AUVs are a relatively new technology, it is also not yet well understood how to best utilize them in oceanographic experimentation. This work addresses the issues inherent in surveying oceanographic phenomena with AUVs and develops quantitative metrics for measuring the effectiveness of these surveys.

The effectiveness of a survey can be addressed quantitatively only within the framework of a given oceanographic experiment. For the purposes of this paper, the objective will be to obtain the best representation, in a least-squares sense, of a measured scalar field. There are two major sources of survey error. One arises from the finite spatial resolution of the survey and the other from the finite time required to sample. Temporal evolution of the ocean during a survey has the effect of "blurring" the reconstructed field [15], driving one to increase vehicle speed and minimize survey distance. However, vehicle speeds are strongly energy constrained, and decreasing the survey distance effectively reduces the sampling resolution (assuming a fixed survey area). Thus, there is a fundamental
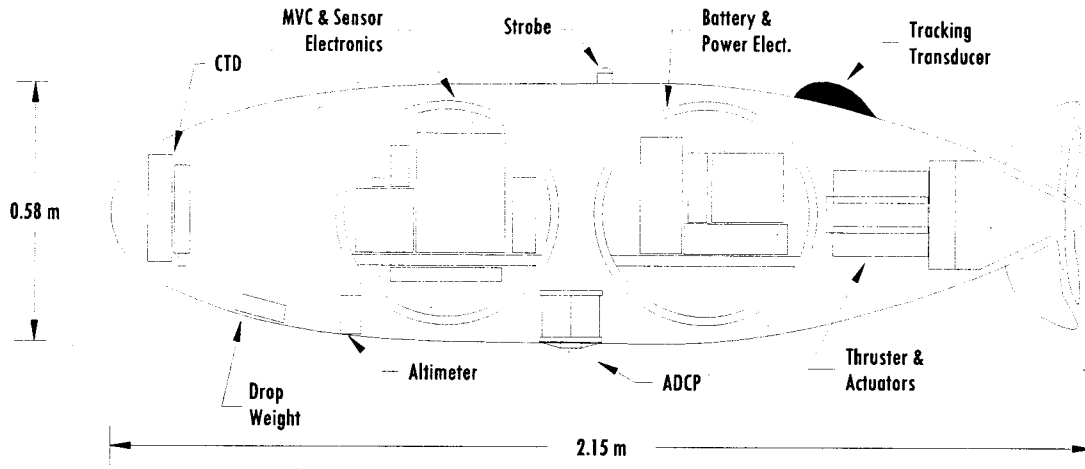
Fig. 1. A schematic of the MIT AUV Laboratory's Odyssey IIb AUV. To date, these 6000-m rated vehicles have completed over 400 deep-ocean and littoral missions. The two glass spheres are the pressure housings for electronics and batteries. The interior of the AUV, where most of the sensors reside, is free-flooded. Equipment not shown includes side-scan sonars, acoustic tomographic sources, DVL, OBS, video cameras, GPS receiver, LBL transponder, and radio and acoustic modems.

tradeoff between errors introduced by temporal evolution or spatial undersampling of the survey field.

An important figure of merit for an oceanographic survey system is the energy required to accomplish a survey [16]. In a practical sense, energy is minimized by reducing the distance a vehicle must travel and optimizing its speed for efficiency. For vehicles which are serviced between missions, perhaps on an oceanographic vessel, there is little incentive to use less than the vehicle's total useful energy capacity in any given mission. However, choices about the consumption of energy are more complex in long-deployment scenarios, such as the autonomous ocean sampling network (AOSN) [17] paradigm, where the bulk of the system's energy may be stored at network nodes rather than in the vehicles themselves. In this case, the tradeoff is between many low-resolution surveys or a few surveys at a higher resolution.

In fact, there are a number of critical tradeoffs which can be made in the design of a grid survey, or in the design of an AUV for a specific oceanographic mission. To aid in making these decisions, certain questions must be answered: What is the best compromise between survey time and resolution? How large an area can be mapped with confidence? How does the survey improve if multiple vehicles are employed? How can current AUVs be improved to enhance their survey performance? These questions are the focus of this paper.

The format of our paper is as follows. In Section II, we review the energy economics of surveying with AUVs and generate a graphical "survey envelope" which is dependent upon the *survey sampling resolution*, λ, and the *total survey time*, τ. Next, we analyze the errors inherent in these surveys as functions of λ and τ and combine these errors to form an overall survey performance metric in Section III. A simple example oceanographic process is employed in Section IV in the development of a graphical survey analysis tool which facilitates quantitative comparisons of differing surveys. Simulations based on the example oceanographic process are used to establish the validity of the combined survey error metric in Section V. In Section VI, we demonstrate the use of our graphical survey analysis plots in an exam-

ination of the impact of certain survey design and AUV parameters on surveys of a simple oceanographic process. We employ the survey analysis plots to optimize a survey of open-ocean deep convection in Section VII. Finally, Section VIII reviews the analysis of the preceding sections, discussing the assumptions made and the utility of our contributions.

II. ENERGY ANALYSIS

A. Energy Consumption

An AUV's energy consumption for a given survey mission is roughly determined by three parameters: the area over which the survey is made, A, the resolution of the survey, λ, and the total time that it takes to complete the survey, τ. Let us consider for the moment a simple grid survey over a fixed square area. The total linear distance, L, traversed in the survey is approximated by

$$L \approx \frac{A}{2\lambda} - 2\lambda \approx \frac{A}{2\lambda} \qquad (1)$$

where 2λ is the distance between tracklines (or points) in a uniform grid survey. The relationship above is clearly only an approximation since the shape and size of the survey relative to the survey resolution must be taken into account. For a rectangular area with both sides significantly larger than λ, the approximation is good. The vehicle speed required to complete such a survey is

$$V = \frac{L}{\tau} \approx \frac{A}{2\lambda\tau} \qquad (2)$$

where τ is the time taken to complete a survey. The total energy consumption [16] for a survey is

$$E_{\text{tot}} = \left[\frac{\rho C_d S V^3}{2\eta} + H\right]\tau \qquad (3)$$

where ρ is the density of water, C_d is the drag coefficient for the vehicle, S is the vehicle's wetted surface area, η is the propulsion efficiency, and H is the vehicle hotel load. Values

TABLE I
PHYSICAL PARAMETERS FOR THE ODYSSEY IIB VEHICLE

Symbol	Value	Description
H	40 W	Hotel Load
η	0.35	Propulsion Efficiency
C_d	0.006	Drag Coefficient
S	3 m	Wetted Surface Area
ρ	1000 kg/m	Density of Water

for these parameters for the standard Odyssey IIb AUV are given in Table I.

The first term in the right hand side of Equation (3) is associated with the propulsion of the vehicle through the water; the second term is the hotel load, i.e., power consumed by electronics, sensor systems, etc. From Equation (3) we see that E_{tot} decreases with decreasing V and/or τ. Since V and τ cannot simultaneously decrease without changing the resolution of the survey, we must tradeoff these two mission parameters to minimize E_{tot}. If we divide the total energy consumed by the total survey distance we have an equation for the energy consumption per unit distance,

$$\frac{E_{\text{tot}}}{L} = \frac{\rho C_d S V^2}{2\eta} + \frac{H}{V}. \tag{4}$$

Taking the derivative of (4) with respect to velocity, V, and setting this equal to zero gives us the optimal vehicle speed

$$V_{\text{opt}} = \left(\frac{H\eta}{\rho C_d S}\right)^{1/3}. \tag{5}$$

This velocity is optimal in the sense that it minimizes energy consumption per unit distance traveled. This relationship indicates that at its optimal speed of 0.92 m/s, the Odyssey IIb class of AUVs will achieve an energy performance of 65.27 J/m, corresponding to a maximum survey path length of approximately 275 km based on a 5-kW-h(1.8×10^7 J) battery pack. Actual range is less (100 km or more) since these vehicles do not typically operate at their optimal speed.

By substituting (5) into (3), we find that the minimum total energy consumption required to complete a grid survey at spatial resolution λ in time τ is

$$E_{\min} = \frac{3LH}{2V_{\text{opt}}} = \frac{3}{2}\tau H. \tag{6}$$

This is a lower bound on the total energy consumed in a time constrained survey.

B. Survey Envelope

In Fig. 2, we compute survey energy consumption for an Odyssey IIb survey of a square survey domain with area $A = (2 \text{ km})^2$. The contours show energy consumption as a function of (λ, τ) over a range which covers current rechargable battery technologies. The dotted line partitions the energy consumption curve into two regions. In the upper region, the total energy consumption is roughly independent of the spatial resolution at which the survey is conducted; these surveys are constrained by the vehicle hotel load. In the lower portion of the plot, both spatial resolution and total survey time influence the
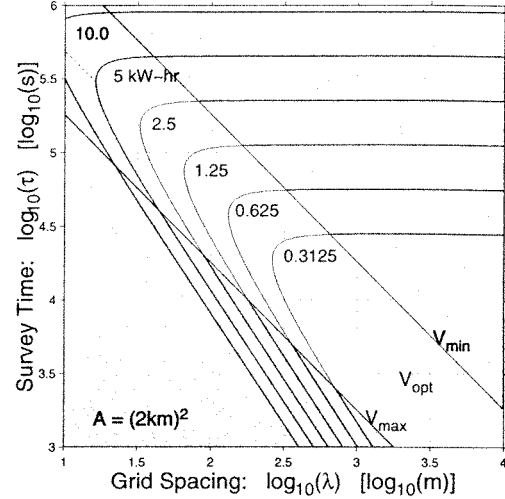

Fig. 2. Total survey energy consumption and survey envelope as a function of survey spatial resolution, λ, and total survey time, τ, for a grid survey of a square survey domain with $A = (2 \text{ km})^2$. Curved lines are energy boundaries (as labeled) and straight lines are vehicle speed constraints ($V_{\min} = 0.25$ m/s and $V_{\max} = 2.5$ m/s). The optimal survey speed ($V_{\text{opt}} = 0.92$ m/s) is shown as a dotted line.

energy consumption of a given survey. As spatial resolution decreases (corresponding to finer grid spacing) the total survey energy increases while total energy consumption increases with decreasing survey time (faster vehicle speed). Typical AUV surveys will be designed to fall into the lower region of the energy consumption curves. We also see that the total survey energy is greatest for surveys which are densely sampled and/or completed quickly.

We must also consider the effects of physical constraints imposed by the AUV on the surveying process. There are three such constraints. For the sake of this example, we have assumed that our AUV has a 5 kW-hr battery. Thus, the total survey energy consumption can be no more than this (1.8×10^7 J). Also, hydrodynamic constraints on the vehicle require that it operate at speeds equal to or greater than 0.25 m/s to maintain control authority. Futhermore, the vehicle has a maximum speed of 2.5 m/s. When taken together, these energy and speed constraints define a finite region of (λ, τ) space within which it is possible for the vehicle to survey. This region, which we refer to as the "survey envelope," is shown in Fig. 2 as the unshaded region. The straight edges of the survey envelope correspond to the AUV speed constraints and the curved edge near the top of the envelope is due to the finite energy stored in the AUV's batteries.

Note that the calculation of total survey energy as a function of (λ, τ), as shown in Fig. 2, assumes a two-dimensional (2-D) survey domain and a uniform grid survey. For a grid survey with a "yo-yo" pattern superimposed in the vertical plane, the total survey distance, and hence, the total survey energy, will increase by a factor

$$f = \cos(\alpha)^{-3} \tag{7}$$

where α is the pitch angle associated with the vehicle's "yo-yo" vertical excursions. As the pitch angle increases, propulsion energy will increase rapidly. There will be some maximum pitch

angle above which the AUV cannot function efficiently due to stability and/or velocity limitations. Note also that a survey trajectory such as this inextricably couples the horizontal and vertical spatial resolutions of the survey. If we wish to sample very densely in a horizontal plane, we will be limited by the maximum pitch angle to very small vertical excursions. For the remainder of this paper, we will consider horizontal survey trajectories only.

III. ERROR ANALYSIS

To assess the degree of synopticity with which an AUV can measure a generic oceanographic process, an understanding of the survey errors inherent in the sampling strategy must be gained. We have identified two major contributions to the survey error, the first being dependent upon the survey's spatial resolution and second on the duration of the survey. In terms of spatial resolution, the survey error is dominated by the loss of detail in the reconstruction of the survey field due the inevitable undersampling of the phenomenon. The dependence of the survey error upon total survey time arises from the evolution of the ocean process over the course of the survey. If we have a reasonable understanding of the physics of the process under study (either from a model or experimental data), we will be able to generate analytic error surfaces in terms of λ and τ for any given survey strategy.

For the following discussion, and throughout the remainder of this paper, our goal will be to accurately reconstruct a "snapshot" of a spatially distributed, time-evolving, scalar parameter process. That is, we want to reconstruct a spatial field which represents, as accurately as possible, the true field at some instance during the survey. The estimated field will exhibit errors due to spatial undersampling and temporal evolution of the underlying phenomenon. For the sake of clarity of analysis, we will assume that any AUV navigational errors are negligible. This assumption is reasonable since navigation errors are typically much smaller than the correlation scales of the ocean process of interest.

A. Spatial Survey Error

Let us begin by considering a spatially distributed process field, $y(\mathbf{x})$, that does not evolve in time. Assume that we have surveyed this field, producing the samples,

$$\hat{y}(\mathbf{x}_i) = y(\mathbf{x}_i) + w(\mathbf{x}_i) \tag{8}$$

where $\mathbf{x}_i$ is the location of the ith sample and $w(\mathbf{x}_i)$ is a zero mean, white measurement noise with variance σ_w^2 and is uncorrelated with $y(\mathbf{x}_i)$. From the noisy samples $\hat{y}(\mathbf{x}_i)$ we reconstruct a continuous field which, for simplicity of notation, we also refer to as $\hat{y}(\mathbf{x})$. This reconstructed field will be bandlimited by the multidimensional equivalent of the Nyquist frequency associated with the survey spatial resolution. We define the error field in terms of the real field and the survey reconstructed field as

$$\varepsilon(\mathbf{x}) = y(\mathbf{x}) - \hat{y}(\mathbf{x}), \qquad \mathbf{x} \in \mathcal{D} \tag{9}$$

where $\mathcal{D}$ is the spatial domain of the survey.

We can define any number of error metrics in terms of this error field. Because the true field $y(\mathbf{x})$ is unknown, we should attempt to determine the expected values for the survey errors instead of absolute survey errors. Accordingly, we have chosen to define our spatial survey error metric to be

$$\varepsilon_\lambda = \frac{E\left\{\int_{\mathcal{D}} |\hat{y}(\mathbf{x}) - y(\mathbf{x})|^2 \, d\mathbf{x}\right\}}{E\left\{\int_{\mathcal{D}} [|\hat{y}(\mathbf{x})|^2 + |y(\mathbf{x})|^2] \, d\mathbf{x}\right\}} \tag{10}$$

which is the expected total energy contained in the error field normalized by the expected total energy contained in the constituent fields so that the spatial survey error will satisfy $0 \leq \varepsilon_\lambda \leq 1$.

We now transform (10) into the Fourier domain by application of the multidimensional version of *Parseval's Theorem* [18] which states that the total energy contained in a signal is proportional to the integral of the squared magnitude of its Fourier transform. Thus, we have

$$\varepsilon_\lambda = \frac{E\left\{\int_{-\infty}^{\infty} |\hat{Y}(\mathbf{k}) - Y(\mathbf{k})|^2 \, d\mathbf{k}\right\}}{E\left\{\int_{-\infty}^{\infty} |\hat{Y}(\mathbf{k})|^2 \, d\mathbf{k} + \int_{-\infty}^{\infty} |Y(\mathbf{k})|^2 \, d\mathbf{k}\right\}}. \tag{11}$$

The value of $|\hat{Y}(\mathbf{k}) - Y(\mathbf{k})|$ is simply the transform of an aliased version of the process field plus some measurement noise and is easy to compute provided that we know the Fourier transform of the process field (e.g., from a model of the process of interest).

The Fourier transforms of the reconstructed field $\hat{Y}(\mathbf{k})$ will be corrupted by spatial aliasing as well as noisy measurements. The effect of aliasing is to fold over spectral energy from wavenumbers higher than the Nyquist wavenumber $\mathbf{k} > \mathbf{k}_s/2$ resulting in increased spectral energy in the recovered field for wavenumbers less that the Nyquist wavenumber, i.e., $\mathbf{k} < \mathbf{k}_s/2$. The effect of the measurement noise is to increase the energy in the reconstructed field uniformly across the wavenumber spectrum. The energy in the error field comes from these two contributions. Thus, we can show [19] that the numerator of (11) is given by

$$E\left\{\int_{\Omega+\Upsilon} |\hat{Y}(\mathbf{k}) - Y(\mathbf{k})|^2 \, d\mathbf{k}\right\}$$
$$= 2\int_{\Omega} |Y(\mathbf{k})|^2 \, d\mathbf{k} + \int_{\Upsilon} |W(\mathbf{k})|^2 \, d\mathbf{k} \tag{12}$$

where $W(\mathbf{k})$ is the Fourier transform of $w(\mathbf{x})$ and we have used the fact that $y(\mathbf{x})$ and $w(\mathbf{x})$ are uncorrelated to separate their Fourier transforms. The regions of integration are

$$\Upsilon = \{\mathbf{k} \,|\, \mathbf{k} \in [-|\mathbf{k}_s|/2, |\mathbf{k}_s|/2]\} \tag{13}$$

which is the support of the sampling process, and

$$\Omega = \{\mathbf{k} \,|\, \mathbf{k} \in [-\infty, -|\mathbf{k}_s|/2) \cup (|\mathbf{k}_s|/2, \infty]\} \tag{14}$$

which is the region of wavenumber space which lies outside the support of the sampling function. Note that Ω and Υ are exclusive sets that partition the whole n-dimensional $\mathbf{k}$-space, i.e., $\Omega \cap \Upsilon = \emptyset$ and $\Omega \cup \Upsilon = \mathcal{R}^n$.

Thus, (11) becomes

$$
\varepsilon_\lambda = \frac{2\int_\Omega |Y(\mathbf{k})|^2\,d\mathbf{k} + \int_\Upsilon |W(\mathbf{k})|^2\,d\mathbf{k}}{2\int_{\Omega+\Upsilon} |Y(\mathbf{k})|^2\,d\mathbf{k} + \int_\Upsilon |W(\mathbf{k})|^2\,d\mathbf{k}}
$$

$$
= \frac{2\int_\Omega \mathcal{P}(\mathbf{k})\,d\mathbf{k} + \int_\Upsilon \mathcal{W}(\mathbf{k})\,d\mathbf{k}}{2\int_{\Omega+\Upsilon} \mathcal{P}(\mathbf{k})\,d\mathbf{k} + \int_\Upsilon \mathcal{W}(\mathbf{k})\,d\mathbf{k}} \qquad (15)
$$

where $\mathcal{P}(\mathbf{k})$ is the energy density spectrum of the process $y(\mathbf{x})$, and $\mathcal{W}(\mathbf{k}) = \sigma_w^2$ is the energy density spectrum for the noise process. We see that as the SNR of the sampling process decreases, the noise terms in the numerator and denominator of (15) dominate, causing $\varepsilon_\lambda \to 1$ as SNR $\to 0$, regardless of the spatial resolution at which the field is sampled. Also, in the absence of measurement noise, undersampling of the true field will cause $\varepsilon_\lambda \to 1$ as the bandwidth of the underlying process increases well beyond the range of the survey spatial resolution, i.e., $|\mathbf{k}_s| \ll |\mathbf{k}_c|$.

Since measurement noise on the typical AUV is quite small in comparison to the signal variance, we will neglect these terms for the remainder of this analysis. Accordingly, we redefine the spatial survey error metric to be

$$
\mathcal{E}_\lambda = \frac{\int_\Omega \mathcal{P}(\mathbf{k})\,d\mathbf{k}}{\int_{\Omega+\Upsilon} \mathcal{P}(\mathbf{k})\,d\mathbf{k}}. \qquad (16)
$$

This metric is a number which ranges between zero and one. It specifies the fraction of the total energy present in the field that we have misassigned in the reconstructed field. For $\mathcal{E}_\lambda = 0$, we have captured all of the energy with the survey and, hence, can perfectly reconstruct the process field.

B. Temporal Survey Error

In the previous section we assumed that the process of interest was static. We now let the process evolve in time. To accurately reconstruct the process at some instant, we would have to make an instantaneous survey. This is analogous to taking a snap-shot of the process and is, of course, impossible to achieve in practice with an AUV. The time evolution of the field will degrade the information which we obtain with our survey. Therefore, we must attempt to determine the degree to which our temporally "blurred" sample field can accurately represent the true field.

For the moment, consider the value of the process field at a single location $\mathbf{x}_i$, at time t, which we will denote with the symbol $y_i(t)$. If the survey begins at time $t = t_o$, then this location would be sampled at some later time, $t = t_o + t'$, due to the finite speed of the AUV. Note that $y_i(t)$ is not a continuous field as was $y(\mathbf{x})$ in Section III-A above. It is rather a collection of random variables at the finite number of spatial sample locations in the survey domain.

To construct a temporal survey error metric, we begin by taking the expectation of the squared error between the true field

value (at time t_o) and survey sample value (at time $t_o + t'$) at the spatial location $\mathbf{x}_i$. This is given by

$$
\begin{aligned}
\varepsilon_{t,\mathbf{x}_i} &= E\left\{[y_i(t_o) - \hat{y}_i(t_o + t')]^2\right\}\\
&= E\left\{y_i^2(t_o) + \hat{y}_i^2(t_o + t') - 2y_i(t_o)\hat{y}_i(t_o + t')\right\}\\
&= \sigma_y^2 + (\sigma_y^2 + \sigma_w^2) - 2\mathrm{cov}(y_i(t_o), y_i(t_o + t')) \quad (17)
\end{aligned}
$$

where σ_y^2 is the temporal variance of the process field and σ_w^2 is the variance of a zero-mean, white noise temporal measurement error which is uncorrelated with the process field. We use the uncorrelatedness of the field and the noise to reduce the last term in the above equation to a covariance function involving only the process field.

From (17) we see that in the absence of measurement noise, $\varepsilon_{t,\mathbf{x}_i} \to 0$ as $t' \to 0$, since the process has no time to evolve before the sample is taken. However, as $t' \to \infty$, (17) goes to $2\sigma_y^2$. We define our normalized point-wise expected error, $\varepsilon_{t'}$, as

$$
\begin{aligned}
\varepsilon_{t'} &= \frac{2\sigma_y^2 - 2\mathrm{cov}(y_i(t_o), y_i(t_o + t')) + \sigma_w^2}{2\sigma_y^2}\\
&= 1 - R(t') + \frac{\sigma_w^2}{2\sigma_y^2} \qquad (18)
\end{aligned}
$$

where we have used the fact that the covariance divided by the variance is defined to be the autocorrelation function, $R(t)$. The last term is a constant which depends on the variance of the measurement noise only. The assumption that $\sigma_y^2 \gg \sigma_w^2$ is typically justifiable and, since the ultimate goal is to gain insight into the effects of λ_s and τ_s on the error metrics, we will ignore this last term in the remainder of the analysis.

Equation (18) computes an expected error for each individual sample in the survey. However, we require an error metric which captures the effect of temporal blurring for all samples in the field. We create this error metric by averaging the point-wise expected errors over the entire survey domain. In the limit, this can be done by integrating (18) over the total survey time, τ_s, and taking the time average. Thus, we use the point-wise error to define the temporal survey error as

$$
\begin{aligned}
\mathcal{E}_\tau &= \frac{1}{\tau_s}\int_{-\tau_s/2}^{\tau_s/2} \varepsilon_{t'}(t')\,dt' = \frac{1}{\tau_s}\int_{-\tau_s/2}^{\tau_s/2} [1 - R(t')]\,dt'\\
&= 1 - \frac{1}{\tau_s}\int_{-\tau_s/2}^{\tau_s/2} R(t')\,dt' \qquad (19)
\end{aligned}
$$

where the time origin, t_o, is placed at the mid-point of the survey to minimize the overall error.

The temporal survey error metric measures the average correlation of the sample field with the true field. As $\tau_s \to 0$, the autocorrelation function will go to one and, hence, $\mathcal{E}_\tau \to 0$. This is as we would expect since we are essentially measuring the difference between two "snap-shots" of the process which have been taken at the same instant. On the other hand, as $\tau_s \to \infty$, $\mathcal{E}_\tau \to 1$ since the autocorrelation function goes to zero, indicating that the sampled field and the field at $t = t_o$ are completely uncorrelated.

C. Combined Survey Error Metric

In the previous two sections, we developed spatial and temporal survey error metrics. The spatial survey error metric gives the expected error in reconstructing a spatial field from an undersampled survey of that field. The temporal survey error metric is an average of pointwise errors derived from the temporal autocorrelation function. We now combine these errors into a single survey error metric,

$$
\begin{aligned}
\mathcal{E}_{tot} &= 1 - (1 - \mathcal{E}_\lambda)(1 - \mathcal{E}_\tau) \\
&= \mathcal{E}_\lambda + \mathcal{E}_\tau - \mathcal{E}_\lambda \mathcal{E}_\tau.
\end{aligned} \tag{20}
$$

In Section III-A, $\mathcal{E}_\lambda$ was interpreted as the fraction of spatial information about the process which has been lost. Therefore, the factor $(1 - \mathcal{E}_\lambda)$ is the fraction of spatial information about the process which has been accurately recovered by the survey. Alternatively, one can think of these quantities as the fraction of detail which has been lost or retained by the sampling process, respectively. The reduction of this information by temporal evolution of the field is given by the second term. Therefore, $\mathcal{E}_{tot}$ measures the uncertainty in our estimate of the process field at time t_o. For $\mathcal{E}_{tot} = 0$, we have a perfect estimate, while $\mathcal{E}_{tot} = 1$ indicates that we have gained no new understanding of the process. Actual surveys will fall between these two extremes.

Recall that both $\mathcal{E}_\lambda$ and $\mathcal{E}_\tau$ are computed from expectations. Implicit in (20) is the assumption that spatial and temporal survey errors are uncorrelated. This assumption will not be valid for many oceanographic processes. Nevertheless, the total survey error metric should be indicative of the gross performance of an AUV survey of these processes and should continue to be useful in designing surveying strategies.

It is also often useful to employ an equivalent characterization of a survey, the overall survey *performance*

$$
P = 1 - \mathcal{E}_{tot} \tag{21}
$$

which also ranges between zero and one and has the obvious interpretation.

IV. SURVEY ANALYSIS PLOTS

To develop the graphical survey analysis plot, we must establish a framework for the process of interest. Let us assume, for the sake of an example, that we wish to survey a slowly evolving, wave-like phenomenon. Let the process of interest be described by a frequency spectral density given by

$$
\mathcal{P}(\omega) = \frac{2\omega_o}{\omega_o^2 + \omega^2} \tag{22}
$$

where $\omega_o = 2\pi/\tau_o$ is the "cutoff" frequency of this Lorentzian density. This density function indicates a process which is dominated by long-wavelength motions and has an exponential autocorrelation function

$$
R(t) = e^{-|t|/\tau_o} = e^{-\omega_o|t|} \tag{23}
$$

where τ_o is the decorrelation time of the example process.

If we further specify that our example field satisfies the plane-wave dispersion relation,

$$
|\mathbf{k}| = \omega/c \tag{24}
$$

where c is the wave propagation speed, then we know that the autocorrelation of the spatial component of the field will also have the exponential form

$$
R(\ell) = e^{-|\ell|/\lambda_o} = e^{-k_o|\ell|}. \tag{25}
$$

Therefore, the spatio–temporal autocorrelation function of the example field is

$$
R(\ell, t) = e^{-k_o(|\ell|+c|t|)}. \tag{26}
$$

Since the process field is spatially isotropic, we can express the spectral density in terms of a scalar radial wavenumber, k. We compute the radial wavenumber spectral density function [20] by taking the Fourier–Bessel transform of the spatial autocorrelation function and multiplying by a factor of $2\pi k$ (assuming a 2-D survey domain). Thus, we have

$$
\begin{aligned}
\mathcal{P}_r(k) &= (2\pi k)\mathcal{P}(\mathbf{k}) \\
&= 2\pi k \left(\frac{1}{2\pi} \int_0^\infty R(\ell) J_o(k\ell) \ell \, d\ell \right) \\
&= \frac{k_o k}{[k_o^2 + k^2]^{3/2}}, \qquad 0 \le k \le \infty
\end{aligned} \tag{27}
$$

where k is the radial wavenumber, $J_0(\cdot)$ is the Bessel function of the first kind of order zero, and $\mathcal{P}(\mathbf{k})$ is the associated (nonradial) wavenumber spectral density of the isotropic random field. Anticipating its later use, we also compute the radial spectral distribution function for the random field

$$
\begin{aligned}
\mathcal{P}_D(k) &= \int_0^k \mathcal{P}_r(\kappa) \, d\kappa \\
&= k_o \int_0^k \kappa [k_o^2 + \kappa^2]^{-(3/2)} \, d\kappa \\
&= 1 - \left[\frac{k_o^2}{k_o^2 + k^2} \right]^{1/2}, \qquad 0 \le k \le \infty.
\end{aligned} \tag{28}
$$

In accordance with the properties on all distribution functions, (28) ranges between zero and one as k ranges from zero to infinity.

We complete the description of the example random field by specifying that it have zero mean ($\mathbf{m}_y = 0$) and unit variance ($\sigma_y^2 = 1$) and that the spatial and temporal correlation scales are $\lambda_o = 512$ m and $\tau_o = 51\,200$ s, respectively, with an equivalent propagation speed of $c = 0.01$ m/s. With these specifications, we can now calculate the spatial and temporal survey errors in addition to the total energy required to complete a survey of this process as functions of the survey parameters (λ_s, τ_s).

A. Spatial Survey Error

Recall from (16) that the spatial survey error is equivalent to the fraction of the total energy of a spatial field which lies out-

side the support of the sampling process. We can easily rewrite (16) in terms of the radial wavenumber spectral density function

$$
\begin{aligned}
\mathcal{E}_\lambda &= \int_{k_s}^{\infty} \mathcal{P}_r(k)\,dk \Big/ \int_0^{\infty} \mathcal{P}_r(k)\,dk \\
&= \mathcal{P}_D(\infty) - \mathcal{P}_D(k_s) \\
&= 1 - \mathcal{P}_D(k_s) \qquad\qquad (29)
\end{aligned}
$$

where $\mathcal{P}_D(k)$ is the wavenumber radial spectral distribution function calculated above and k_s is one-half the sampling density (i.e., the Nyquist density).

The distribution function is a monotonic function which measures the fractional amount of the total spectral energy contained in wavenumbers up to the sampling density, k_s. Therefore, $\mathcal{E}_\lambda$ is also a monotonically increasing function of k_s. Inserting (27) into (29) gives the spatial survey error for this example process

$$
\mathcal{E}_\lambda = \left[\frac{k_o^2}{k_o^2 + k_s^2}\right]^{1/2} = \left[\frac{\lambda_s^2}{\lambda_o^2 + \lambda_s^2}\right]^{1/2}, \qquad 0 \le \lambda_s \le \infty. \quad (30)
$$

B. Temporal Survey Error

We now turn our attention to the temporal survey error. Inserting (23) in to (19), the temporal survey error for our example process is

$$
\begin{aligned}
\mathcal{E}_\tau &= \frac{1}{\tau_s} \int_{-\tau_s/2}^{\tau_s/2} \left[1 - e^{-|t|/\tau_o}\right] dt \\
&= 1 + \frac{2\tau_o}{\tau_s}\left(e^{-\tau_s/2\tau_o} - 1\right). \qquad (31)
\end{aligned}
$$

C. Combined Survey Error

Finally, we combine the spatial and temporal survey errors to form the combined survey error, $\mathcal{E}_{\text{tot}}$. Inserting (30) and (31) into (20), we obtain

$$
\begin{aligned}
\mathcal{E}_{\text{tot}}(\lambda_s, \tau_s) &= \left[1 + \frac{2\tau_o}{\tau_s}\left(e^{-\tau_s/2\tau_o} - 1\right)\right] \\
&\quad - \frac{2\tau_o}{\tau_s}\left[\frac{\lambda_s^2}{\lambda_o^2 + \lambda_s^2}\right]^{1/2}\left(e^{-\tau_s/2\tau_o} - 1\right) \qquad (32)
\end{aligned}
$$

This quantity is plotted in Fig. 3 as a function of normalized sampling density (λ_s/λ_o) and normalized survey time (τ_s/τ_o). Note that the error contour lines are more closely spaced on the spatial resolution axis than on the total survey time axis. This is a consequence of the fact the spatial error accounts for errors in two spatial dimensions whereas the temporal survey error accrues errors only in a single dimension.

D. Survey Analysis Plots

We have used (32) to generate a plot of the combined survey error as a function of survey spatial resolution and total survey time for our example ocean process. Fig. 3 indicates that surveys which are sampled quickly and densely have minimal survey error. However, as we saw in Section II, fast and dense surveys also correspond to high energy consumption. A tradeoff between energy consumption and the combined survey error must be made to obtain optimal survey parameters.
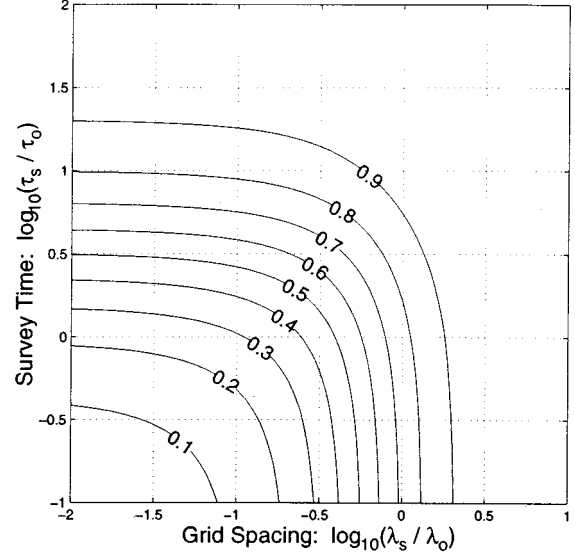

Fig. 3. Combined survey error as a function of (λ_s, τ_s) for a grid survey of the example process $(\lambda_o = 512$ m and $\tau_o = 51\,200$ s$)$ in a survey domain of area, $A = 4$ km^2. Minimal error is achieved for surveys which are sampled densely and quickly. Conversely, $\mathcal{E}_{tot} \to 1$ for coarse and slow surveys, indicating that very little information about the process field has been recovered.

If we combine the survey envelope with the combined survey error by directly superimposing Figs. 2 and 3, we generate a plot, Fig. 4, which indicates the survey errors achievable for all combinations of the survey parameter pair, (λ_s, τ_s) achievable by an Odyssey IIb AUV surveying our example process. Plots such as these are what we have termed the "survey analysis plot." They allow us to make objective judgments about the various issues involving survey design and/or AUV design parameters. For instance, using Fig. 4, we can readily determine the minimum error, $\mathcal{E}_{\min} = 0.162$, which can be achieved with the Odyssey IIb AUV for this particular survey example. Surveying at any combination of (λ_s, τ_s) other than those specified by this minimum value will result in decreased survey efficiency.

V. SIMULATION AND VALIDATION

Before moving on to applications of the survey analysis plots, we now revisit the combined survey error metric to explore its accuracy by comparing it to survey errors from surveys of a simple simulated ocean field. The simulations are based on the technique of sampling from the spectrum [21]. This technique generates isotropic spatial random fields by taking a normalized sum of several harmonic components at each point in the simulation. The wavenumbers which define these harmonic components are themselves random variables which are distributed in accordance with the radial spectral distribution of the desired random field. A simple modification of this technique allows it to be extended to time-varying processes. Perhaps the most important feature of this simulation technique is the ability to calculate simulated values at any location within the field at any instance in time. This capability is required for surveys which follow irregular survey trajectories.

In the following sections, the technique of sampling from the spectrum will be reviewed for spatial random fields. Simulated surveys from the resulting fields will be conducted and recon-
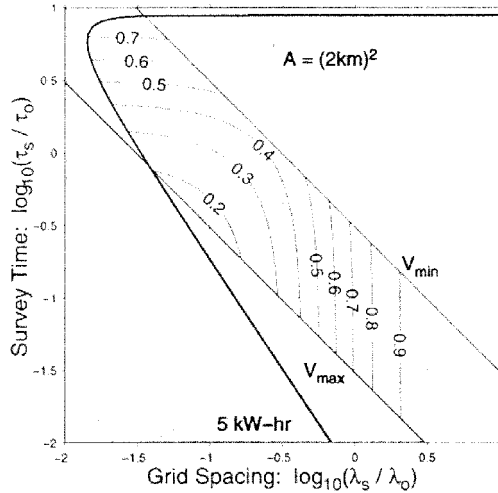
Fig. 4.   Survey analysis plot as a function of (λ_s, τ_s) for our example process with $\lambda_o = 512$ m and $\tau_o = 51\,200$ s. The combination of the survey envelope and combined survey error forms a tool which can be used to optimize surveys in terms of various survey parameters. Each point within the survey envelope gives the expected combined survey error for a particular (λ_s, τ_s) pair. The minimum error possible for the present example is $\mathcal{E}_{\min} = 0.162$.

struction errors from these surveys will be compared to the combined survey error metric of Section III.

A. Process Simulation

For clarity of exposition and for computational simplicity, we have chosen to simulate a time-varying, 2-D, random field, $y(\mathbf{x}, t)$, which is spatially homogeneous and isotropic and temporally stationary. Furthermore, the simulated fields will have zero mean, $\mathbf{m}_y = 0$, and unit variance, $\sigma_y^2 = 1$. We have also chosen to use a separable exponential autocovariance function

$$R(\ell, t) = R(\ell)R(t) = e^{-2\pi|\ell|/\lambda_\circ} e^{-2\pi|t|/\tau_\circ} \qquad (33)$$

where ℓ is the (scalar) distance between two points in the field, i.e., $\ell = |\mathbf{x}|$. Given our zero-mean and unit variance assumptions, we see that the autocovariance function is equivalent to the autocorrelation function of the random field. The spatial correlation length is denoted by λ_0, and τ_o is the temporal correlation "length," or time constant. The corresponding wavenumber-frequency spectrum of the process will be a separable function of k and ω,

$$\mathcal{P}_r(k, \omega) = \mathcal{P}_r(k)\mathcal{P}(\omega) \qquad (34)$$

where $\mathcal{P}_r(k)$ denotes the radial wavenumber energy density spectrum (we have relied upon the fact that the desired random field is spatially isotropic in order to write the wavenumber spectrum as a function of a scalar wavenumber k).

We see from (27) as well as the zero mean and unit variance assumptions that the statistics of the spatial random field are completely determined by the length scale parameter, λ_o. Thus, simulation of a spatial random field begins by choosing a length scale for the desired field and then selecting a vector of random wavenumbers from which the spatial random field will be formed. The way in which these random wavenumbers are selected is known as sampling from the spectrum and it is

this process which gives the simulation technique its name. This method is as follows.

Let $\mathbf{u} \in \mathcal{R}^M$ be a random vector with elements u_i uniformly distributed on $[0, 1]$. Furthermore, let each element satisfy the equation

$$u_i = \mathcal{P}_D(k_i) \qquad (35)$$

where the (scalar) radial wavenumbers, k_i, are the random wavenumbers which we seek. We solve for these wavenumbers by taking the inverse of (35)

$$k_i = \mathcal{P}_D^{-1}(u_i). \qquad (36)$$

Finally, this vector of random wavenumbers is used to simulate a zero mean, unit variance spatial random field

$$y(x_1, x_2) = \sqrt{\frac{2}{M}} \sum_{i=1}^{M} \cos[k_i(x_1 \cos\alpha_i + x_2 \sin\alpha_i + ct) + \theta_i] \qquad (37)$$

where the α_is are random directions uniformly distributed on $[0, 2\pi)$ and the θ_is are random phases also uniformly distributed on $[0, 2\pi)$. We have employed the dispersion relation (24) to write random frequencies in terms of the random wavenumbers, k_i. Thus, the 2-D spatial random field consists of a collection of M plane progressive waves of random wavelength and phase, each oriented in a random direction. It is easily shown that the simulated fields have zero mean and unit variance, are spatially homogeneous and isotropic and temporally stationary [19]. The simulations can be modified so that the resulting random fields are anisotropic by allowing the radial wavenumber spectral density/distribution to be parameterized by the random directions, α_i, in addition to the parameter u_i.

B. AUV Survey Simulations

Using the simulation technique described above, we have generated simulated AUV surveys of spatially varying, temporally evolving processes. These surveys implement a simple grid pattern over a square domain. The *true* field is calculated on a 128×128 cell grid which spans the simulation domain. The survey begins at time $t_o - \tau_s/2$ and ends at time $t_o + \tau_s/2$. The *true* field is the instantaneous spatial field at the time $t = t_o$.

The AUV survey fields are generated as follows: A spatial trajectory for a grid survey is computed and discretized on a square, uniform grid. Beginning at the southwest corner of the simulation domain at time $t = t_o - \tau_s/2$, the field is sampled in the first cell. At each subsequent sampling instant, $t_n = t_o - \tau_s/2 + n\Delta t$, a value is taken at the corresponding location in the simulation domain. These spatially and temporally distributed sample values build up a random field at a spatial resolution equal to or coarser than the true random field. The time between sample points, Δt, is dependent upon the speed of the AUV, the length of the survey trajectory, and the granularity of the spatial grid. Thus, the effects of temporal blurring and spatial aliasing will be present in the sampled field. Spatial interpolation is performed with a bi-cubic spline method to place the reconstructed field on the same spatial grid as the true field.

C. Survey Simulation Errors

The prime motivation for implementing the simulation process is to facilitate the verification of the combined survey error metric developed in Section III. We now explore the correspondence between this theoretical error metric and the errors from time-varying and spatially-aliased simulated AUV surveys. In each experiment the simulated survey errors are defined to be the normalized mean square of the difference between the field reconstructed from the simulated survey samples and the *true* field. This mean square error is normalized by the energy contained in the reconstructed and true fields. Thus, we have

$$\mathcal{E}_{sim} = \frac{\sum_i [y(\mathbf{x}_i, t_o) - \hat{y}(\mathbf{x}_i, t_i)]^2}{\sum_i [y^2(\mathbf{x}_i, t_o) + \hat{y}^2(\mathbf{x}_i, t_i)]} \quad (38)$$

where $y(\mathbf{x}_i, t_o)$ is the true field, $\hat{y}(\mathbf{x}_i, t_i)$ is the reconstructed field, $\mathbf{x}_i$ ranges over all sample locations in the true field, and t_o is the sampling instance in the middle of the simulated AUV survey (t_o may be set to zero without loss of generality).

Fig. 5 shows the overall survey performance from these simulated surveys (recall that the survey performance is simply one minus the combined survey error). We have varied both the spatial resolution, λ_s, and the total survey time, τ_s, of the simulated AUV surveys in such a way so as to cut a diagonal across the (λ, τ) space. The mean of the overall survey performances from an ensemble of sixteen surveys is shown as an open circle for each combination of (λ, τ). The variance of the overall performance metric and hence of the combined survey error metric is indicated by ± 1 standard deviation bars. The good agreement between the simulation and theoretical (solid line) performances validates the combined survey error metric of Section III.

VI. APPLICATIONS

There are numerous internal and external parameters which effect the performance of an AUV survey of an oceanographic process. Internal variables which influence AUV survey performance are factors such as the capacity of the vehicle's battery, the efficiency of its propulsion system, the vehicle's hotel load, and its maximum speed. The three external parameters which have the greatest impact upon the overall survey performance are: 1) the ratio of the survey spatial resolution to the characteristic length scale (correlation distance) of the process of interest, (λ_s/λ_o); 2) the ratio of the total survey time to the time constant (correlation time) of the process, (τ_s/τ_o); and 3) the size of the survey domain, A. The complex interconnections of these internal and external parameters compound the difficulties of designing field experiments which make extensive use of AUVs. The survey analysis plot of Section IV was developed as an aid in sorting out these interconnections. In this section, we will demonstrate the application of survey analysis plots to this task. The example random process of Section IV provides the necessary context for these analyses.
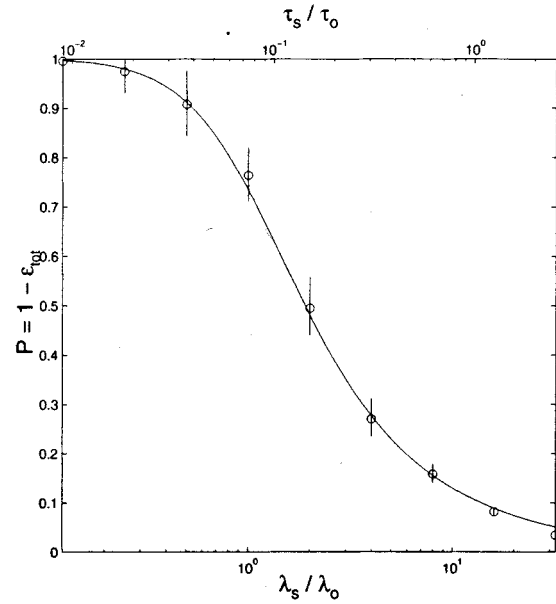

Fig. 5. Overall survey performance from simulated surveys (open circles) compared to the theoretical performance metric (solid line). One standard deviation error bars are shown.

A. Survey Design

In this section we explore the effects of the three external parameters on the overall survey performance through the application of the survey analysis plot. We have previously shown how survey analysis plots can be used to select the (λ_s, τ_s) pair which gives the minimum survey error for our example process. We now revisit this idea. In Figs. 6(a), 4, and 6(b), we show analysis plots for our example process with domains of varying size, $A = (3 \text{ km})^2$, $(2 \text{ km})^2$, and $(1 \text{ km})^2$, respectively. In each of these plots, minimum survey errors (Table II) lie in the region along the lower left corner of the survey envelope. This is a consequence of the fact that one must sample densely and quickly to achieve small errors. The fact that errors lie along the boundaries of the survey envelope indicates either that all of the vehicle's energy has been consumed (curvelinear portions of the boundary) or that the vehicle has reached its maximum speed constraint (linear portions of the boundary) in attaining this minimum error. Note also that the minimum error is strongly tied to the area of the survey domain; smaller errors will be achieved in smaller survey domains. As shown in Table II, the size of the survey domain is the first parameter which one should choose when designing an AUV field program since this choice has the greatest impact on the overall survey performance.

Having made the choice of survey domain size, one should then determine the number of surveys be made. If the generation of a high-resolution "snap-shot" of the process of interest is the overriding objective of the experiment, then a single survey which achieves a small error is desired. However, if coarser surveys can be tolerated, then perhaps multiple surveys are in order.

These survey analysis plots indicate that a continuum of surveys are possible for any given value of $\mathcal{E}_{tot}$ (except in the case $\mathcal{E}_{tot} = \mathcal{E}_{min}$). For instance, the surveys along the curve $\mathcal{E}_{tot} = 0.3$ tradeoff spatial resolution against total survey time
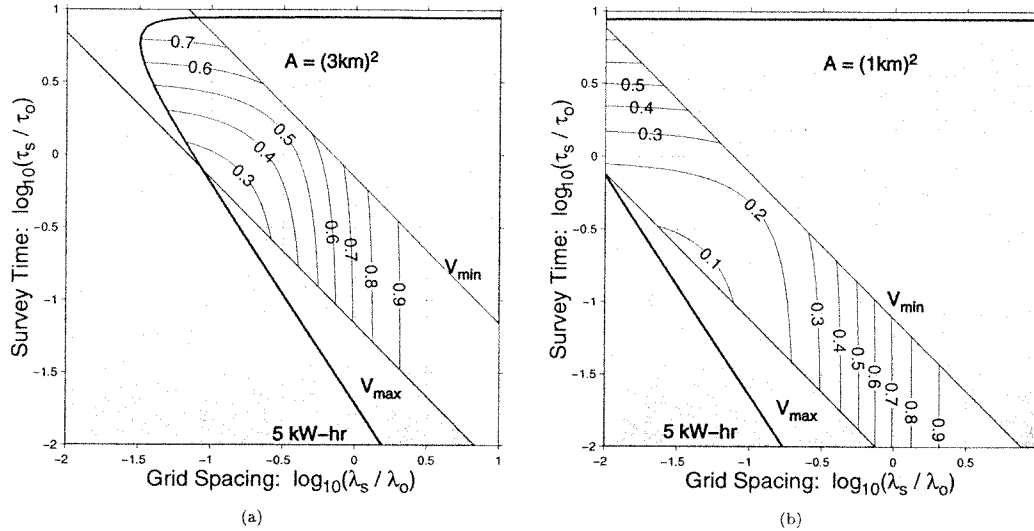
Fig. 6.   Survey analysis plots for surveys domains of varying area. The size of the survey domain is $A = (3 \text{ km})^2$ in (a) and $A = (1 \text{ km})^2$ in (b). Compare with Fig. 4 where $A = (2 \text{ km})^2$. These figures demonstrate the effect of changing the overall size of the survey domain on combined survey errors. Minimum survey errors for each plot are given in Table II.

TABLE II
COMBINED SURVEY ERRORS FOR SURVEYS WITH DOMAINS OF VARYING SIZE

Area	$\mathcal{E}_{min}$	Figure
$A = (3\text{km})^2$	0.242	Figure 6(a)
$A = (2\text{km})^2$	0.162	Figure 4
$A = (1\text{km})^2$	0.086	Figure 6(b)

to maintain a constant value for the combined survey error. Considering only the two surveys lying at the intersection of the curve $\mathcal{E}_{\text{tot}} = 0.5$ with the boundaries of the survey envelope, we see that one of these surveys will be as fast as possible but will have poor spatial resolution. The other survey will have fine spatial resolution but will take a long time to complete. The slow but densely sampled survey is constrained by the size of the vehicle's battery while it is the AUV's maximum speed which limits the fast but coarsely sampled survey. In fact, after reviewing Fig. 2, we see that the fast but coarse survey consumes only about half of the available energy, leaving open the possibility of a second survey. Again, the researcher must make a choice regarding the utility of differing survey strategies using the insight gained from the application of the survey analysis plots.

B. Vehicle Design

We now employ the survey analysis plots to gain insight into the effects of the previously mentioned internal parameters on the overall performance of an AUV survey. In Fig. 7, survey analysis plots are shown for surveys of the example process by modified Odyssey IIb vehicles. All of these surveys were conducted over a domain of area $A = (2 \text{ km})^2$. These plots illustrate the effects of modifying various vehicle parameters on overall survey performance. The minimum survey errors for these surveys are given in Table III. See Fig. 4 to compare these plots with that for an unmodified Odyssey IIb vehicle. We discuss the effects of modifying the vehicle parameters below:

1) Reduced Hotel Load: In Fig. 7(a), the vehicle's hotel load, H, is reduced to 1/2 of its Odyssey IIb value. Comparing with Fig. 4, we see that decreasing the hotel load changes the shape of the survey envelope by pushing the envelope's energy boundary toward the upper left corner of the plot, allowing longer duration surveys. However, this does not result in a reduction in the minimum survey error over that of the unmodified Odyssey IIb survey since, in this example, the minimum error is determined by the vehicle speed constraint. The minimum survey error is the same as that for the unmodified AUV, $\mathcal{E}_{\min} = 0.162$.

2) Increased Propulsion Efficiency: In Fig. 7(b), the vehicle's propulsion inefficiency, $(1 - \eta)$, is reduced to 1/2 of its previous value, resulting in an overall increase in propulsion efficiency. This pushes the energy boundary of the survey envelope toward the left side, allowing more densely sampled surveys. Since the minimal survey error is constrained by the maximum vehicle speed, the minimum survey error does not change. However, these surveys do consume less energy. This can be beneficial if the field program requires multiple survey missions to be completed by the vehicle.

3) Increased Maximum Velocity: Next, the AUV's maximum speed is increased by a factor of two. As shown in Fig. 7(c), this pushes the maximum speed constraint directly toward the lower left corner, allowing both faster and more densely sampled surveys. Recalling that energy consumption goes as the cube of the vehicle speed [Equation (3)], it is not surprising that the energy boundary portion of the survey envelop now constrains the minimum survey error. The minimum error is reduced by approximately 14 percent, $\mathcal{E}_{\min} = 0.139$.

4) Multiple Vehicle Surveys: Because it is quite difficult in general to increase an AUV's maximum speed without increasing its size or moving to a different energy source (such as combustion engines or fuel cells), we examine the use of multiple vehicles in Fig. 7(d). Two unmodified Odyssey IIb vehicles are employed in these surveys. Since two vehicles can cover twice the distance in unit time as can one vehicle,
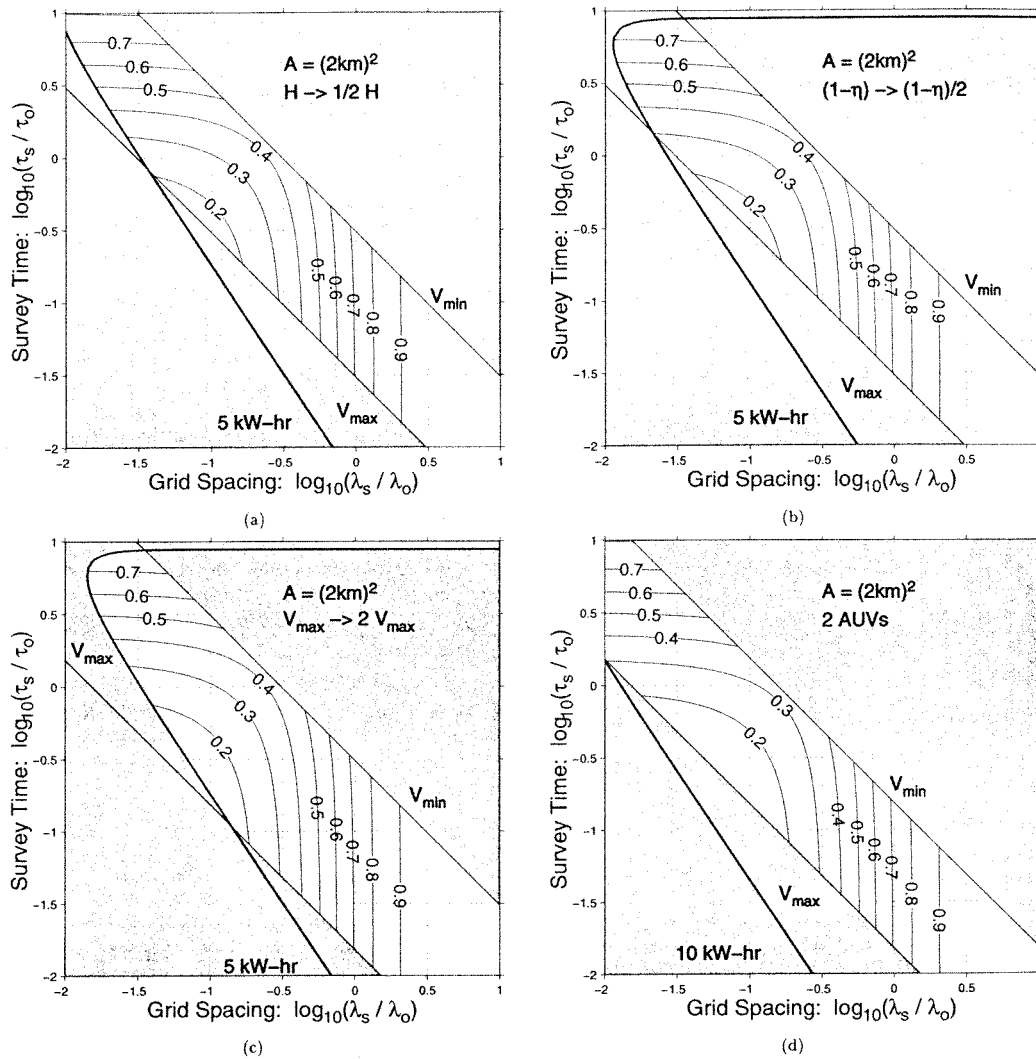
Fig. 7. Survey analysis plots for modified vehicle parameters in a survey domain of area $A = (2\text{ km})^2$. (a) The vehicle's hotel load, H, is reduced to 1/2 of the standard Odyssey IIb value. (b) The vehicle's propulsion inefficiency, $(1 - \eta)$, is reduced to 1/2 of its previous value. (c) The maximum vehicle speed is doubled. (d) Two standard Odyssey IIb vehicles are employed in this survey. Compare with the analysis plot for an unmodified Odyssey IIb, Fig. 4. Minimum survey errors are given in Table III

TABLE III
COMBINED SURVEY ERRORS FOR AUVS WITH MODIFIED VEHICLE
PARAMETERS

Area	Parameter	$\mathcal{E}_{min}$	Figure
$(2\text{km})^2$	Unmodified	0.162	4
$(2\text{km})^2$	H, η	0.162	7(a), 7(b)
$(2\text{km})^2$	Fast Vehicle	0.139	7(c)
$(2\text{km})^2$	Two AUVs	0.116	7(d)

the survey speed is effectively doubled. Also, the two AUVs have twice the battery capacity of a single AUV and the energy portion of the survey envelope is expands toward the left side of the plot. Unlike the case of the fast vehicle above, the energy boundary is not adversely impacted by the effective increase in survey speed. The maximum speed constraint is again the limiting factor or survey performance. The minimum survey error is significantly reduced: $\mathcal{E}_{\min} = 0.116$.

Using analysis plots, one is able to objectively compare the various AUV platforms to determine which platform is best suited to a specific scientific program or field experiment. The

analysis plots can also be employed by the vehicle designers to guide them in making crucial tradeoffs during the initial phases of a new vehicle design. For existing vehicles, the above analysis indicates that certain design modifications would not be beneficial to the overall survey performance. For instance, our analysis for the Odyssey IIb AUV indicates that, if reducing the combined survey error is the overriding goal, then it is more beneficial to design and build several low-cost AUVs than to focus on reducing hotel load, wetted surface area, or propulsion inefficiency.

In this section, we have demonstrated the use of the survey analysis tool in guiding the survey and vehicle design processes. In the following section we will apply the survey analysis tool to the design of an AUV survey of an oceanographic process of current interest.

VII. APPLICATION TO OPEN-OCEAN DEEP CONVECTION

Open-ocean deep convection plays a key role in ocean circulation by mixing surface water with deeper water, thus re-
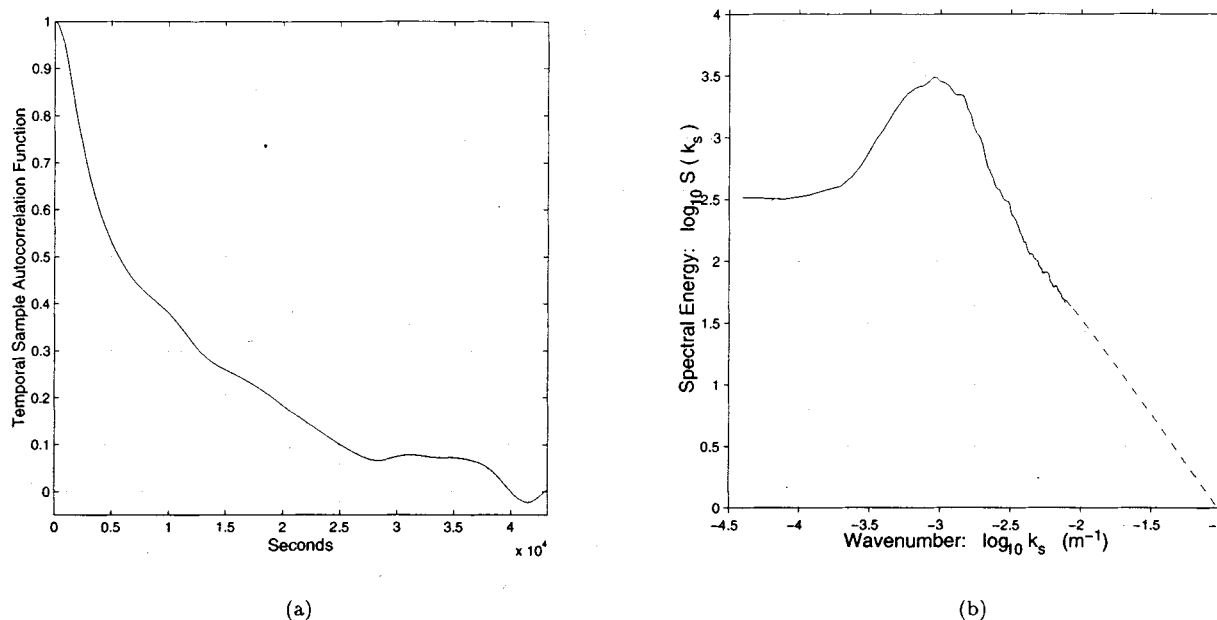
(a)

(b)

Fig. 8.   Open-ocean deep convection statistics. (a) The temporal sample autocorrelation function is calculated from observations of an open-ocean deep convection model [22]. The temporal sample autocorrelation decays to zero after approximately 12 h and the e^{-1} decorrelation time is 175 min. (b) A wavenumber spectral density estimate is also calculated from observations of the convection model. Here, a slice through the isotropic spectrum is shown. The characteristic wavelength corresponding to the broad spectral peak is 1000 m. This distance is the characteristic separation between convective plumes. The high wavenumber portion of the spectrum (dashed line) was chosen to be consistent with the spectrum at adjacent wavenumbers.

newing the intermediate and deep waters of the world's oceans. It is most likely to occur during prolonged winter storms when the surface heat flux (cooling by low air temperature and gales) is largest. Labrador Sea is one of only a few deep convection locations in the world, along with the Greenland Sea and several locations around Antarctica. Owing to its importance, the Labrador Sea has been intensively studied in the last few years [23].

Open-ocean deep convection has been simulated by John Marshall and his group at the Department of Earth, Atmospheric, and Planetary Sciences, Massachusetts Institute of Technology, using a nonhydrostatic numerical model [22]. Data from this model was used to estimate the temporal autocorrelation function and wavenumber spectral density of the process. An estimate of the model's temporal autocorrelation function for vertical water velocity is shown in Fig. 8(a). The autocorrelation function has a maximum time lag of 12 h with granularity of 30 s and was calculated as an average of time-series observations at 192 fixed locations throughout the model domain. The decorrelation time is 175 min and the autocorrelation function decays to zero after approximately 12 h. To calculate the horizontal wavenumber spectral density of the vertical velocity field, the model was allowed to evolve for 14 h, at which time the convection has become well established. We sampled a horizontal plane at a depth of 500 m every 30 min for the final 4 h of the simulation. From each of these observations, individual horizontal wavenumber spectral estimates were calculated and then averaged and smoothed to produce the spectral estimate. A slice through the resulting isotropic spectrum is shown in Fig. 8(b). The spectral peak corresponds to a wavelength of 1000 m, this being the characteristic separation between convective plumes. The spatial structure of the convection process is dominated by

long-wavelength motions which are well resolved by the 50-m grid spacing of the numerical model. These space and time scales are typical of the real process.

Let us now assume, for the sake of an example, that we wish to grid survey over a fixed, square area, $A = (1 \text{ km})^2$, using an Odyssey IIb AUV. By numerical integration of (16), (19), and (20), we combine the spatial and temporal survey errors and calculate the combined survey error, shown as a function of survey time and grid spacing in Fig. 9(a). As expected, Fig. 9(a) indicates that minimum error surveys are accomplished rapidly, and with fine spatial resolution. Given the relatively short mission times required by the temporal autocorrelation (slightly less than three hours) and a maximum speed constraint on the vehicle of 2.5 m/s, missions are not constrained by battery capacity. Consequently, the important survey constraint for this example is maximum vehicle speed. For the open-ocean deep convection example with a survey area of one square kilometer, the minimum survey error is $\mathcal{E}_{\min} = 0.220$, Fig. 9(b). Decreasing the area covered by the survey or increasing the number of AUVs used in the survey allows the survey error to be reduced significantly. In Fig. 9(c), we have reduced the total survey region to $A = (1/2 \text{ km})^2$. This has the effect of changing the error surface underlying the survey envelope, resulting in a minimum survey error of $\mathcal{E}_{\min} = 0.086$. Alternatively, if we use three AUVs to survey the original survey area, $A = (1 \text{ km})^2$, we can again lower the combined survey error, Fig. 9(d). In this case, the minimum survey error is $\mathcal{E}_{\min} = 0.116$.

From the survey analyses of Fig. 9, we can better appreciate the tradeoffs necessary in surveying open-ocean deep convection using an AUV. For example, since the characteristic distance between convective plumes is approximately 1000 m, the minimum error survey of Fig. 9(c) would give acceptable performance if the scientific objective were to make an accurate es-
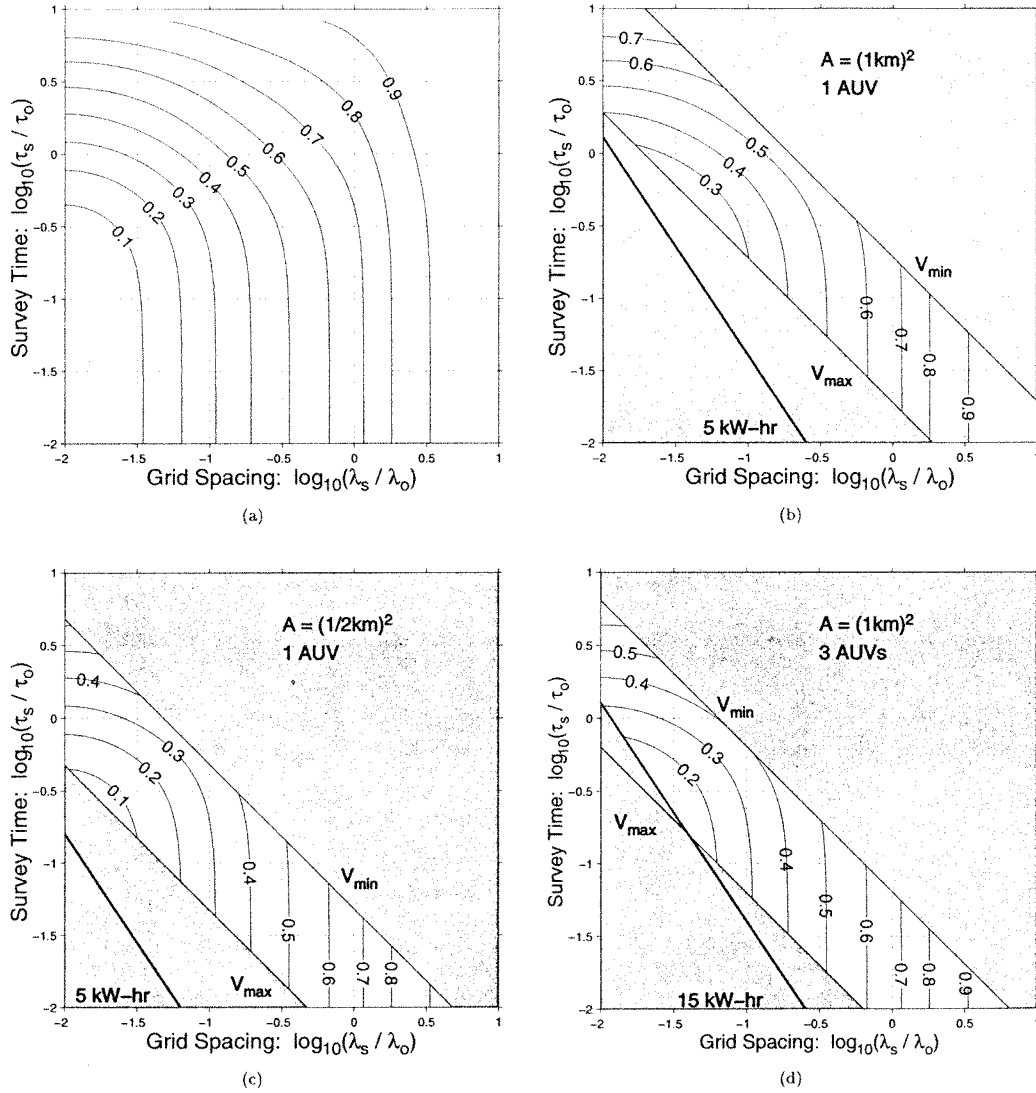
Fig. 9. Survey analyses for open-ocean deep convection. (a) Combined survey error as a function of (λ, τ). (b) Survey analysis plot for a survey of a square domain of area $A = (1 \text{ km})^2$. (c) Survey analysis plot for a of area $A = (1/2 \text{ km})^2$. The survey envelope translates downward, giving access to surveys with lower total error. (d) Survey analysis plot for three Odyssey IIb AUVs surveying a domain of area $A = (1 \text{ km})^2$. Minimum survey errors for these surveys are given in Table IV.

TABLE IV
MINIMUM SURVEY ERRORS FOR SURVEYS OF OPEN-OCEAN DEEP CONVECTION

Area	$\mathcal{E}_{min}$	Figure
$(1\text{km})^2$	0.220	9(b)
$(1/2\text{km})^2$	0.086	9(c)
$(1\text{km})^2$	0.116	9(d)

timate of the vertical heat within the interior of a single plume. Alternatively, if the mission goal is gather information about the distribution or formation of the convective plumes, then the minimum error surveys of Fig. 9(b) and (d) or ones over even larger survey domains would be more appropriate.

VIII. CONCLUSION

In this work, we have explored the problem of reconstructing spatially distributed, time evolving process fields with samples from AUV surveys. We have developed survey performance metrics which quantify vehicle energy consumption and both spatial and temporal survey errors and have validated these metrics within a simulation environment. We have also used these performance metrics to gain insight into the design of AUV surveys of oceanographic processes and to identify useful ways to customize the design of an AUV in light of particular scientific objectives. The contributions of this paper to the general problem of surveying with AUVs place the survey design problem firmly within a quantitative framework. However, modifications of and improvements upon this work are certainly possible and will be needed as the use of AUVs in oceanographic and other settings grows and matures. Our contributions are reviewed below.

1) Performance Metrics: In Section II, we reviewed the energy economics of surveying with AUVs and created the survey "envelope" which quantifies AUV energy consumption for a given survey domain in terms of the survey's spatial resolution,

λ_s, and the total survey time, τ_s. We also explored the errors inherent in reconstructing a spatial field from temporally blurred survey samples, Section III. Two error metrics were developed, one of which measures the error due to spatial undersampling of the phenomenon of interest. The second metric estimates the errors due to the temporal evolution of the process field over the course of the survey. These error metrics were combined into a single total survey error metric. In developing these metrics, we made several simplifying assumptions in order to make the problem tractable or to simplify the presentation. These assumptions were the following.

1) The process of interest is temporally stationary and spatially homogeneous, but not necessarily spatially isotropic.
2) The frequency and wavenumber spectra (or, equivalently, the spatial and temporal autocorrelation functions) of the process of interest were assumed to be known.
3) Errors due to AUV positional uncertainties are negligible, i.e., uncertainties in the position of the AUV are much smaller than the spatial resolution scale of the survey. This is reasonable given an external navigational aid such as an acoustical long-baseline system, which can give positional uncertainties as low as 1–10 m [24].
4) The process of interest was assumed to be the only oceanographic phenomenon at play in the survey region. This assumption excludes, for example, ocean currents and tides.
5) Errors due to the finite extent of the AUV surveys (i.e., truncation errors) were also assumed to be negligible. While this may be a reasonable assumption for densely gridded surveys, it will be an increasingly poor assumption for low-resolution surveys as the number of tracklines across a survey domain decreases.
6) The efficiency of the AUV's propulsion system was assumed to be constant over a wide range of vehicle speeds.
7) We have also assumed that the AUVs sample the process of interest in a square grid pattern. This was done so that the survey envelope and survey error metrics could be visualized on 2-D plots for the sake of clarity of exposition and does not reflect a limitation of the spatial survey error metric.

Problems that meet the above assumptions can be addressed within the framework of error metrics developed in Section III.

2) Survey Analysis Plots: The survey envelope of Section II was combined with the combined survey error metric of Section III to create a graphical survey analysis tool, Section IV. These plots elucidate the tradeoffs between survey resolution, total survey time, and the size of the survey domain. The minimum error survey for an example problem was identified.

3) Simulation and Validation: In Section V, we implemented a simple space-time random field simulation based on the method of sampling from the spectrum. This technique is powerful in that it does not require unnecessary computation and is flexible in terms of the size and shape of the survey domain as well as its ability to compute field values along arbitrary space–time survey trajectories. We employed these simulated surveys in the verification of the survey error metric

of Equation (20) and found good agreement between the errors from the simulated surveys and the theoretical errors.

4) Survey Analyses: Survey analysis plots were applied to the analysis of AUV surveys of random fields in Section VI. These analyses gave insight into the process of survey sampling with AUVs. Several tradeoffs of spatial resolution versus total survey time were discovered and their implications for AUV survey design were discussed. We demonstrated the optimization of a uniform grid survey over a square domain of a simple random process field. The values for the spatial resolution, λ_s, and total survey time, τ_s, indicated by this analysis were shown to be optimal in the sense that they minimized the expected survey error while constraining the survey to lie within the survey envelope.

Finally, we employed the survey performance metrics in an analysis of several vehicle design parameters and considered the use of several AUVs to conduct a single survey. Not surprisingly, we found that methods which allow an AUV to move more quickly through the water give the most dramatic decreases in total survey error. *Using multiple vehicles was found to be the most beneficial and straightforward methods of improving overall survey performance.*

REFERENCES

[1] T. D. Dickey, "The emergence of concurrent high-resolution physical and bio-optical measurements in the upper ocean and their applications," *Rev.Geophys.*, vol. 29, no. 3, pp. 383–413, Aug. 1991.
[2] D. R. Blidberg and G. Sedor, "An interdisciplinary workshop to assess the scientific needs for a long range autonomous underwater vehicle," Tech. Rep., Marine Systems Eng. Lab., University of New Hampshire, 1991.
[3] J. G. Bellingham, C. A. Goudey, T. R. Consi, J. W. Bales, D. K. Atwood, J. J. Leonard, and C. Chryssostomidis, "A second generation survey AUV," in *Proc. IEEE Conf. Autonomous Underwater Vehicles*, Cambridge, MA, 1994.
[4] S. M. Smith and S. E. Dunn, "The Ocean Voyager II: An AUV designed for coastal oceanography," in *Proc. IEEE Conf. Autonomous Underwater Vehicles*, Cambridge, MA, 1994.
[5] C. von Alt, B. Allen, T. Austin, and R. Stokey, "Remote environmental measuring units," in *Proc. IEEE Conf. Autonomous Underwater Vehicles*, Cambridge, MA, 1994.
[6] J. G. Bellingham, "New oceanographic uses of autonomous underwater vehicles," *Marine Technol. Soc. J.*, vol. 31, no. 3, pp. 34–47, 1997.
[7] D. R. Yoerger, A. M. Bradley, B. B. Walden, H. Singh, and R . Bachmayer, "Surveying a subsea lava flow using the Autonomous Benthic Explorer (ABE)," *Int. J. Syst. Sci.*, vol. 29, no. 10, pp. 1031–1044, 1998.
[8] D. R. Yoerger, A. Bradley, R. Bachmayer, R. Catanach, A. Duester, S. Liberatore, H. Singh, and B. Walden, "Near-bottom magnetic surveys of the coaxial ridge segment using the Autonomous Benthic Explorer survey vehicle," *RIDGE Events*, vol. 7, no. 1, 1996.
[9] S. Willcox, J. Vaganay, and J. Rish, "The Bluefin BPAUV: An organic wide-area bottom mapping and mine-hunting platform," in *Proc. 12th Int. Symp. on Unmanned Untethered Submersible Technology*, Aug. 2001.
[10] E. Burian, D. Yoerger, A. Bradley, and H. Singh, "Gradient search with autonomous underwater vehicles using scalar measurements," in *Proc. IEEE Symp. Autonomous Underwater Vehicle Technology*, Monterey, CA, June 1996, pp. 86–98.

[11] E. R. Levine, R. G. Lueck, R. R. Shell, and P. Licis, "Coastal turbulence estimates and physical process studies utilizing a small AUV," in *Proc. 11th Int. Symp. Unmanned Untethered Submersible Technology*, Aug. 1999, pp. 94–102.

[12] J. S. Willcox, "A real-time framework for adaptive tomographic surveys without vertical line arrays," in *Proc. 11th Int. Symp. Unmmanned Untethered Submersible Technology*, Aug. 1999, pp. 299–310.

[13] S. Tiwari, "Mosaicking of the ocean floor in the presence of three-dimensional occlusions in visual and side-scan sonar images," in *Proc. IEEE Symp. Autonomous Underwater Vehicle Technology*, Monterey, CA, June 1996, pp. 308–314.

[14] B. S. Bourgeois, A. B. Martinez, P. J. Alleman, J. J. Cheramie, and J. M. Gravley, "Autonomous bathymetry survey system," *IEEE J. Ocean Eng.*, vol. 24, pp. 414–423, Oct. 1999.

[15] P. A. Mathews, "The impact of nonsynoptic sampling on mesoscale oceanographic suryveys with towed instruments," *J. Atmos. Oceanic Technol.*, vol. 14, pp. 162–174, Feb. 1997.

[16] A. M. Bradley, "Low power navigation and control for long range autonomous underwater vehicles," in *Proc. 2nd Int. Offshore and Polar Eng. Conf.*, San Francisco, CA, June 1992.

[17] T. B. Curtin, J. G. Bellingham, J. Catipovic, and D. Webb, "Autonomous oceanographic sampling networks," *Oceanography*, vol. 6, no. 3, pp. 86–94, 1993.

[18] D. E. Dudgeon and R. M. Mersereau, *Multidimensional Digital Signal Processing*. Englewood Cliffs, NJ: Prentice-Hall, 1984.

[19] J. S. Willcox, "Oceanographic surveys with autonomous underwater vehicles: Performance metrics and survey design," master's thesis, Massachusetts Institute of Technology, Feb. 1998.

[20] R. L. Bras and I. Rodriguez-Iturbe, *Random Functions and Hydrology*. Mineola, NY: Dover , 1993.

[21] J. M. Mejia and I. Rodriguez-Iturbe, "On the sythesis of random field sampling from the spectrum: An application to the generation of hydrologic spatial processes," *Water Resources Res.*, vol. 10, no. 4, pp. 705–711, 1974.

[22] H. Jones and J. Marshall, "Convection with rotation in a neutral ocean: A study of open-ocean deep convection," *J. Phys. Oceanogr.*, vol. 23, pp. 1009–1039, June 1993.

[23] The Lab Sea Group, "The Labrador Sea deep convection experiment," *Bull. Amer. Meteor. Soc.*, vol. 79, no. 10, pp. 2033–2058, Oct. 1998.

[24] J. Vaganay, J. G. Bellingham, and J. J. Leonard, "Comparison of fix computation and filtering for autonomous acoustic navigation," *Int. J. Syst. Sci.*, vol. 29, no. 10, pp. 1111–1122, 1998.

James G. Bellingham received the M.S., and Ph.D. degrees in physics, from the Massachusetts Institute of Technology (MIT), Cambridge, MA, in 1984, and 1988, respectively.

He spent the last thirteen years developing Autonomous Underwater Vehicles (AUV), first as Manager of the MIT Sea Grant College Program AUV Laboratory and, more recently, as the Director of Engineering at the Monterey Bay Aquarium Research Institute (MBARI). He has worked in areas ranging from vehicle design, to high-level control, to field operations. His primary contribution is the creation of the Odyssey class of AUVs with which he has led operations in areas as remote as the Arctic and Antarctic. In the area of high-level control, he developed state-configured layered control, a new methodology for handling mission-level control of autonomous vehicles.

Dr. Bellingham is a founder and member of the Board of Directors of Bluefin Robotics Corporation, a leading manufacturer of AUVs for the military, commercial, and scientific markets.

Yanwu Zhang (S'95–M'00) was born in June 1969 in Shaanxi Province, China. He received the B.S. degree in electrical engineering and the M.S. degree in underwater acoustics engineering from Northwestern Polytechnic University, Xi'an, China, in 1989 and 1991, respectively, the M.S. degree in electrical engineering and computer science from the Massachusetts Institute of Technology (MIT), Cambridge, and the M.S. degree in oceanographic engineering from the MIT/Woods Hole Oceanographic Institution (WHOI) Joint Program, both in 1998, and the Ph.D. degree in oceanographic engineering from the MIT/WHOI Joint Program in 2000.

From June to December 2000, he was a Systems Engineer working on medical image processing at the General Electric Company Research and Development Center, Niskayuna, NY. Since January 2001, he has been a Digital Signal Processing (DSP) Engineer in the Research and Development Division of Aware Inc., Bedford, MA, working on digital communications. His research interests are in spatio-temporal signal processing, autonomous underwater vehicles, and digital communications. He had two papers published in IEEE Journal of Oceanic Engineering and IEEE TRANSACTIONS ON NEURAL NETWORKS. He also served as a reviewer for the above two journals and the *Journal of Atmospheric and Oceanic Technology*.

Dr. Zhang is a member of Sigma Xi.

Arthur B. Baggeroer (S'62–M'68–SM'87–F'89) received the B.S.E.E. degree from Purdue University, West Lafayette, IN, in 1963, and the Sc.D. degree from the Massachusetts Institute of Technology (MIT), Cambridge, MA, in 1968.

He is a Ford Professor of Engineering in the Department of Ocean Engineering and the Department of Electrical Engineering and Computer Science at MIT. He has also been a consultant to the Chief of Naval Research at the NATO SACLANT Center in 1977 and a Cecil and Ida Green Scholar at the Scripps Institution of Oceanography in 1990 while on sabbatical leaves. His research has been concerned with sonar array processing, acoustic telemetry, and most recently, global acoustics and matched field array processing. He also has had a long affiliation with the Woods Hole Oceanographic Institution (WHOI) and was Director of the MIT/WHOI Joint Program from 1983 to 1988.

Dr. Baggeroer is a Fellow of the Acoustical Society of America, and he was elected to the National Academy of Engineering in 1995. He was awarded the Secretary of the Navy/Chief of Naval Operations Chair in Oceanographic Science in 1998.

J. Scott Willcox (S'97–M'00) received the B.S. degree in electrical engineering and the M.S. degrees in ocean engineering and in electrical engineering from the Massachusetts Institute of Technology, Cambridge, in 1993 and 1998, respectively, where he is now a Ph.D. candidate in the Department of Ocean Engineering.

His research interests include adaptive AUV survey strategies, AUV navigation, and AUV-based acoustic tomography. Since September of 1999, he has served as the Technical Manager for Bluefin Robotics Corp., a leading manufacturer of military, commercial, and scientific AUVs.

Mr. Willcox is a member of the Society of Naval Architects and Marine Engineers.